



# Synthesis of ternary Ag/ZnO/ZnFe<sub>2</sub>O<sub>4</sub> porous and hollow nanostructures with enhanced photocatalytic activity

Shikui Wu<sup>a,b</sup>, Xiaoping Shen<sup>a,\*</sup>, Guoxing Zhu<sup>a</sup>, Hu Zhou<sup>c</sup>, Zhenyuan Ji<sup>a</sup>, Kangmin Chen<sup>a</sup>, Aihua Yuan<sup>c</sup>

<sup>a</sup> School of Chemistry and Chemical Engineering, School of Material Science and Engineering, Jiangsu University, Zhenjiang 212013, PR China

<sup>b</sup> Inner Mongolia Medical University, College of Pharmacy, Hohhot 010059, PR China

<sup>c</sup> School of Material Science and Engineering, School of Environmental and Chemical Engineering, Jiangsu University of Science and Technology, Zhenjiang 212003, PR China

## ARTICLE INFO

### Article history:

Received 17 September 2015

Received in revised form

14 November 2015

Accepted 22 November 2015

Available online 28 November 2015

### Keywords:

Zinc ferrite

Ternary composite

Hollow nanostructure

Synthesis

Photocatalysis

## ABSTRACT

Highly uniform Ag/ZnO/ZnFe<sub>2</sub>O<sub>4</sub> ternary composites with porous and hollow nanostructures are synthesized using Ag-loaded Prussian blue analogue Zn<sub>3</sub>Fe(CN)<sub>6</sub>·xH<sub>2</sub>O (Ag-ZnPBA) as the precursor via a facile calcination process. The cubic morphology of the precursor is well inherited after the calcination process. The microstructures of the ternary composites can be tuned from porous to hollow interiors by simply changing the heating modes. The loading amount of Ag in the composites can be adjusted by controlling the initial adsorption amount of Ag<sup>+</sup> ions on the metal-organic framework of ZnPBA. The as-synthesized ternary Ag/ZnO/ZnFe<sub>2</sub>O<sub>4</sub> shows significantly enhanced photocatalytic activity towards the degradation of organic dye as compared to the binary counterpart of ZnO/ZnFe<sub>2</sub>O<sub>4</sub>, demonstrating the important role of Ag for the photocatalytic process. It seems that the combination of the three components of Ag, ZnO, ZnFe<sub>2</sub>O<sub>4</sub> can form type-II band alignment and Schottky barrier, which would inhibit the recombination of photo-generated electrons and holes. Moreover, benefited from the excellent magnetic property of ZnFe<sub>2</sub>O<sub>4</sub>, the composite photocatalysts can be easily recovered from reaction systems by a magnet. This work presents a facile and effective route for the construction of uniform multi-component nanocomposites with intriguing structures and multiple functions.

© 2015 Elsevier B.V. All rights reserved.

## 1. Introduction

Spinel zinc ferrite (ZnFe<sub>2</sub>O<sub>4</sub>) with a narrow bandgap of 1.9 eV is considered to be a potential candidate for visible-light-driven photocatalysts due to its very high sensitivity to sunlight, excellent photochemical stability, low toxicity and superior magnetic separable property [1–3]. Recently, some efforts have been devoted to develop nanostructured ZnFe<sub>2</sub>O<sub>4</sub> photocatalysts [4,5]. Nanoscale particles with smaller sizes and larger specific surface areas can shorten the diffusion distance of photogenerated carriers transferring to the surface of photocatalysts, and increase the surface catalytic active sites, which are beneficial for improving photocatalytic efficiency [6]. However, the interior electron-hole recombination ratio would increase in nanostructured materials because the abundant defects in such materials can act as carrier traps and recombination centers [7,8]. As a result, nanoscaled

ZnFe<sub>2</sub>O<sub>4</sub> itself usually shows rather poor photocatalytic activities [9–11]. It is known that coupling a p-type semiconductor with a suitable n-type one to form type-II band alignment could drive the photogenerated electrons and holes to transfer towards opposite directions, thereby minimizing their recombination [12]. Recently, Guo et al. reported a composite photocatalyst consisting of p-type ZnFe<sub>2</sub>O<sub>4</sub> and n-type ZnO, which exhibits remarkably enhanced photocatalytic activity [13]. In addition, loading noble metals such as Ag as a co-catalyst on oxide semiconductors is another promising route to suppress electron-hole recombination [14]. For example, it was reported that the binary composites of Ag/ZnFe<sub>2</sub>O<sub>4</sub> and Ag/ZnO both show enhanced photocatalytic activities compared to single phase ZnFe<sub>2</sub>O<sub>4</sub> or ZnO [1,15]. Accordingly, modification of ZnFe<sub>2</sub>O<sub>4</sub> with ZnO and Ag to form ternary composites would be highly desirable to further improve the photocatalytic performance. Regrettably, such Ag/ZnO/ZnFe<sub>2</sub>O<sub>4</sub> ternary catalysts have not been reported so far, probably due to the great synthesis challenge.

Metal-organic frameworks (MOFs) are a kind of porous materials consisting of metal ions or clusters coordinated to organic

\* Corresponding author. Fax: +86 511 88791800.  
E-mail address: [xiaopingshen@163.com](mailto:xiaopingshen@163.com) (X. Shen).

ligands. They have wide applications in adsorption, gas storage and catalysis due to their high surface areas and tunable porosities. Recently, MOFs have been used as a new class of precursors for synthesizing porous oxide materials through simple calcination processes [16–19]. With this strategy, microstructures and pore dimensions of the resulted oxide materials can be easily tuned by controlling the thermal treatment conditions such as temperature and heating rate [20,21]. However, the compositions are usually limited by the specific MOF precursors. As important members of MOFs family, Prussian blue (PB) and its analogues (PBAs) have recently been demonstrated to be highly effective precursors for porous mono- or bi-component metal oxides [22–27]. For example, Lou's group synthesized  $\text{Fe}_2\text{O}_3$  microboxes with hierarchically structured shells and excellent lithium storage property by simply annealing PB microcubes [25]. Chen et al. prepared a series of porous metal oxides such as  $\text{Co}_3\text{O}_4$  nanocages [26],  $\text{Mn}_x\text{Co}_{3-x}\text{O}_4$  nanocubes [23] and  $\text{ZnO}/\text{Co}_3\text{O}_4$  porous spheres [27] by calcinating  $\text{M}_3^{II}[\text{Co}(\text{CN})_6]_2 \cdot x\text{H}_2\text{O}$  ( $\text{M} = \text{Co}, \text{Mn}, \text{Zn}$ ) precursors. And Jiang et al. prepared nanoporous  $\text{ZnFe}_{2-x}\text{O}_4$ - $\text{ZnO}$  binary composite by calcinating  $\text{K}_2\text{Zn}_3[\text{Fe}(\text{CN})_6]_2 \cdot x\text{H}_2\text{O}$  microplates at  $500^\circ\text{C}$  [19]. However, it is difficult to obtain porous composite materials with more than two components because of the composition limitation of PBAs precursors.

In this work, we demonstrate the preparation of highly uniform  $\text{Ag}/\text{ZnO}/\text{ZnFe}_2\text{O}_4$  ternary catalysts with porous and hollow nanostructures using Ag-loaded Prussian blue analogue  $\text{Zn}_3\text{Fe}(\text{CN})_6 \cdot x\text{H}_2\text{O}$  (ZnPBA) as the precursor. The Ag-ZnPBA precursor was obtained through an adsorption process in  $\text{Ag}^+$  solution. The Ag content of  $\text{Ag}/\text{ZnO}/\text{ZnFe}_2\text{O}_4$  composites can be easily adjusted by controlling the initial adsorption amount of  $\text{Ag}^+$  ions on ZnPBA. The as-synthesized  $\text{Ag}/\text{ZnO}/\text{ZnFe}_2\text{O}_4$  ternary nanostructures show excellent photocatalytic performance towards the degradation of organic dye of methylene blue (MB). The semiconductor band alignment ( $\text{ZnO}/\text{ZnFe}_2\text{O}_4$ ) and Schottky barrier ( $\text{Ag}/\text{ZnO}$ ) in this structure are considered to play the key roles for the significantly improved photocatalytic activity.

## 2. Experimental

### 2.1. Synthesis

All chemicals were of analytical grade and used without further purification. Deionized water was used throughout this study.

#### 2.1.1. $\text{Zn}_3\text{Fe}(\text{CN})_6 \cdot x\text{H}_2\text{O}$ (ZnPBA) cubes

50 mL of  $\text{ZnCl}_2$  solution (6 mM) and 1.0 mL of  $\text{HCl}$  solution (12 M) were added into 50 mL of  $\text{K}_3\text{Fe}(\text{CN})_6$  solution (4 mM). The resulted solution was stirred at room temperature for 30 min, and then aged in dark for 6 h. The generated precipitate was collected by centrifugation, washed several times with deionized water and ethanol, respectively, and then dried in a vacuum oven at  $60^\circ\text{C}$  for 12 h.

#### 2.1.2. Ag-loaded $\text{Zn}_3\text{Fe}(\text{CN})_6 \cdot x\text{H}_2\text{O}$ (Ag-ZnPBA) cubes

In a typical synthesis, 1.5 mL of  $\text{AgNO}_3$  solution ( $1 \text{ mg mL}^{-1}$ ) was added into the aqueous dispersion of ZnPBA nanocubes (100 mg in 50 mL of  $\text{H}_2\text{O}$ ). After stirring for 2 h, the product was collected by centrifugation, washed several times with deionized water and ethanol, and then dried in a vacuum oven at  $60^\circ\text{C}$  for 12 h.

#### 2.1.3. Conversion of Ag-ZnPBA nanocubes to porous $\text{Ag}/\text{ZnO}/\text{ZnFe}_2\text{O}_4$ nanocubes

Ag-ZnPBA nanocubes were calcined in air at  $500^\circ\text{C}$  for 4 h with a heating rate of  $10^\circ\text{C min}^{-1}$ . After cooled to room temperature naturally, the porous  $\text{Ag}/\text{ZnO}/\text{ZnFe}_2\text{O}_4$  product was collected and denoted as p-Ag/ $\text{ZnO}/\text{ZnFe}_2\text{O}_4$ .

#### 2.1.4. Conversion of Ag-ZnPBA nanocubes to hollow $\text{Ag}/\text{ZnO}/\text{ZnFe}_2\text{O}_4$ nanocubes

The Ag-ZnPBA nanocubes were first heated to  $200^\circ\text{C}$  with a heating rate of  $2^\circ\text{C min}^{-1}$ , and maintained at this temperature for 1 h in air atmosphere. Then, the temperature was elevated to  $500^\circ\text{C}$  with a heating rate of  $1^\circ\text{C min}^{-1}$  and kept at this temperature for 4 h. After cooled to room temperature naturally, the hollow  $\text{Ag}/\text{ZnO}/\text{ZnFe}_2\text{O}_4$  cubes were collected and designated as h-Ag/ $\text{ZnO}/\text{ZnFe}_2\text{O}_4$ .

### 2.2. Instruments and characterization

The phase structures of the as-prepared products were characterized using powder X-ray diffraction (XRD, Rigaku D/MAX 2400) with  $\text{Cu-K}\alpha$  radiation ( $\lambda = 1.5406 \text{ \AA}$ ) at a scanning rate of  $2^\circ\text{C min}^{-1}$ . The size, morphology and microstructure of the samples were characterized by scanning electron microscopy (SEM, JSM-6480), field emission scanning electron microscopy (FESEM, JSM-7001F) and transmission electron microscopy (TEM, JEOL JEM-2100). The compositions of the products were determined using an energy-dispersive X-ray spectrometer (EDX) attached to SEM.  $\text{N}_2$  adsorption-desorption isotherms were obtained at 77 K on a Coulter SA 3100 surface area analyzer. Ultraviolet-visible (UV-vis) spectroscopy measurements were performed with a UV-2450 UV-vis spectrophotometer. Elemental mapping images were acquired on a Tecnai G2 F30 S-Twin TEM.

### 2.3. Photocatalytic measurements

Photocatalytic activities of the as-synthesized products were evaluated by the degradation of MB solution under simulated sunlight irradiation. A 250 W Xe lamp was positioned at ca. 10 cm away from the reaction cell to trigger the photocatalytic reaction. There is a water layer between the reaction system and the lamp to remove the thermal effect of light. The experiments were performed at room temperature as follows: 50 mg of the photocatalyst was added to 100 mL of MB solution ( $10 \text{ mg L}^{-1}$ ) in a Pyrex reactor. Before illumination, the suspension was stirred in the dark for 30 min to ensure the establishment of an adsorption-desorption equilibrium between the photocatalyst and MB solution. The dispersion was then exposed to the light irradiation under stirring. At given time intervals, 4 mL of the suspension was pipetted into a centrifuge tube and centrifuged at 8000 rpm for 2 min to remove the remnant photocatalyst. The concentrations of MB solution in the supernatant were monitored by checking the absorbance at 664 nm using the UV-vis spectrophotometer. Total organic carbon (TOC) was measured using a TOC analyzer (Analytik Jena AG multi N/C 2100). The degree of mineralization was calculated based on the TOC percent removal rate, according to the expression:

$$\% \text{Mineralization} = \frac{(\text{TOC}_0 - \text{TOC}_t)}{\text{TOC}_0} \times 100\%$$

where  $\text{TOC}_0$  is the initial TOC of the synthetic solution and  $\text{TOC}_t$  is its value at reaction time  $t$ . All experiments were carried out in duplicate and only the mean values were reported.

### 2.4. Photoelectrochemical characterization

The photoelectrochemical characteristics were measured in a CHI750D electrochemical workstation (Chen Hua Instruments, Shanghai, China) using a standard three compartment cell under the light irradiation (500 W Xe lamp). Typically, 15 mg of the as-prepared samples was added into a mixture containing 5 mL of ethanol, 0.05 mL oleic acid and 1 mg of Polyvinyl pyrrolidone (PVP), and then magnetically stirred for 24 h. The viscous paste was then coated on a piece of  $1 \text{ cm} \times 2 \text{ cm}$  FTO glass. After dried at  $45^\circ\text{C}$ , they

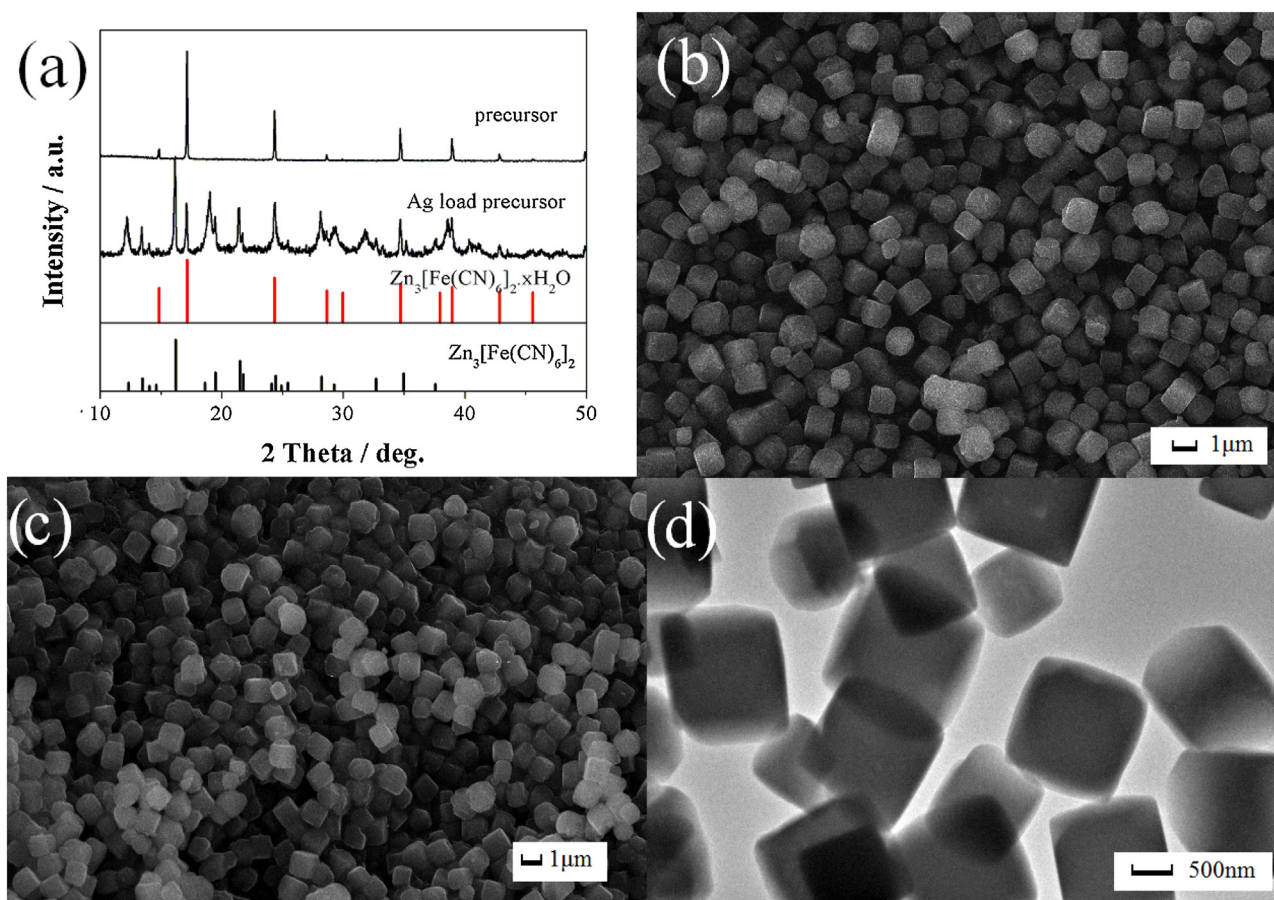


**Fig. 1.** (a) XRD patterns of the as-synthesized ZnPBA and Ag-ZnPBA. The standard XRD patterns of  $\text{Zn}_3[\text{Fe}(\text{CN})_6]_2 \cdot x\text{H}_2\text{O}$  and  $\text{Zn}_3[\text{Fe}(\text{CN})_6]_2$  are also given for comparison. (b) SEM image of ZnPBA. (c) SEM and (d) TEM images of Ag-ZnPBA.

were calcinated at  $500^\circ\text{C}$  for 30 min to remove the PVP and oleic acid. The obtained FTO glass coated with the samples was then used as working electrode for photoelectrochemical measurement. A Pt electrode and a saturated calomel electrode (SCE) were used as the counter electrode and the reference electrode, respectively.  $\text{Na}_2\text{SO}_4$  (0.5 M) aqueous solution was employed as an electrolyte.

### 3. Results and discussion

#### 3.1. Synthesis and characterization

XRD patterns of the as-synthesized ZnPBA and Ag-ZnPBA nanocubes are shown in Fig. 1a. All the detectable peaks of ZnPBA are consistent with the standard data of face-centered cubic (fcc)  $\text{Zn}_3[\text{Fe}(\text{CN})_6]_2 \cdot x\text{H}_2\text{O}$  (JCPDS 38-0687), indicating that the synthesized product is well-crystallized  $\text{Zn}_3[\text{Fe}(\text{CN})_6]_2 \cdot x\text{H}_2\text{O}$  without detectable impurities. While for the XRD pattern of Ag-ZnPBA, besides the diffraction peaks attributable to  $\text{Zn}_3[\text{Fe}(\text{CN})_6]_2 \cdot x\text{H}_2\text{O}$ , all the other diffraction peaks can be well indexed to fcc  $\text{Zn}_3[\text{Fe}(\text{CN})_6]_2$  (JCPDS 25-1022). This result suggests that the silver ions could replace some water molecules in the lattice of ZnPBA, which is consistent with the cases reported for MOFs adsorption of heavy metal ions such as  $\text{Pb}^{2+}$ ,  $\text{Cu}^{2+}$  and  $\text{Ni}^{2+}$  [28,29]. Fig. 1b shows the SEM image of the ZnPBA product. It can be seen that the ZnPBA is composed of well-defined cubes with a size of ca.  $1\ \mu\text{m}$ . After ZnPBA adsorption for  $\text{Ag}^+$  ions, the morphology and size of the resulted Ag-ZnPBA product do not show obvious change (Fig. 1c and d), suggesting the cubic structure is well maintained after doping. In

addition, the surface of the cubes is smooth. No obvious defects or voids were observed on the surface (Fig. 1d).

The as-prepared Ag-ZnPBA precursor can be transformed into porous or hollow Ag/ZnO/ZnFe<sub>2</sub>O<sub>4</sub> cubes by calcination in air. The morphologies and microstructures of the final products were examined by FESEM and TEM. As shown in Fig. 2a and b, the samples of *p*-Ag/ZnO/ZnFe<sub>2</sub>O<sub>4</sub> and *h*-Ag/ZnO/ZnFe<sub>2</sub>O<sub>4</sub> show similar cubic morphology to the original Ag-ZnPBA precursor. However, the surfaces of the cubes become rather rough, and some broken cubes can be observed. TEM images (Fig. 2c and e) of *p*-Ag/ZnO/ZnFe<sub>2</sub>O<sub>4</sub> confirm that cubes were transformed to porous ones after the one-step fast heating process. The size of the porous cubes is about  $1\ \mu\text{m}$ . Interestingly, the hollow cubes of *h*-Ag/ZnO/ZnFe<sub>2</sub>O<sub>4</sub> were obtained through a two-step slow heating process (Fig. 2d). The hollow cubes with a hollow interior show a size of about  $1\ \mu\text{m}$  and a shell thickness of about 20 nm. From the HRTEM images (Fig. 2e and f), clear lattice fringes can be observed. The lattice fringes with spacings of 0.487, 0.26 and 0.23 nm can be indexed to the (1 1 1) crystallographic planes of cubic phase ZnFe<sub>2</sub>O<sub>4</sub>, the (0 0 0 2) planes of hexagonal ZnO, and the (1 1 1) planes of cubic Ag, respectively, revealing that the cubes are composed of ZnFe<sub>2</sub>O<sub>4</sub>, ZnO and Ag nanoparticles. Moreover, there are many irregular pores between the particles, revealing the porosity of the cubes. The insets in Fig. 2e and f show the corresponding fast Fourier transform (FFT) patterns of *p*-Ag/ZnO/ZnFe<sub>2</sub>O<sub>4</sub> and *h*-Ag/ZnO/ZnFe<sub>2</sub>O<sub>4</sub>, which further confirm the presence of ZnFe<sub>2</sub>O<sub>4</sub>, ZnO and Ag in the composites.

XRD measurements were performed to further confirm the phase variation from the Ag-ZnPBA precursor to the calcinated products. Fig. 3 displays the XRD patterns of the obtained



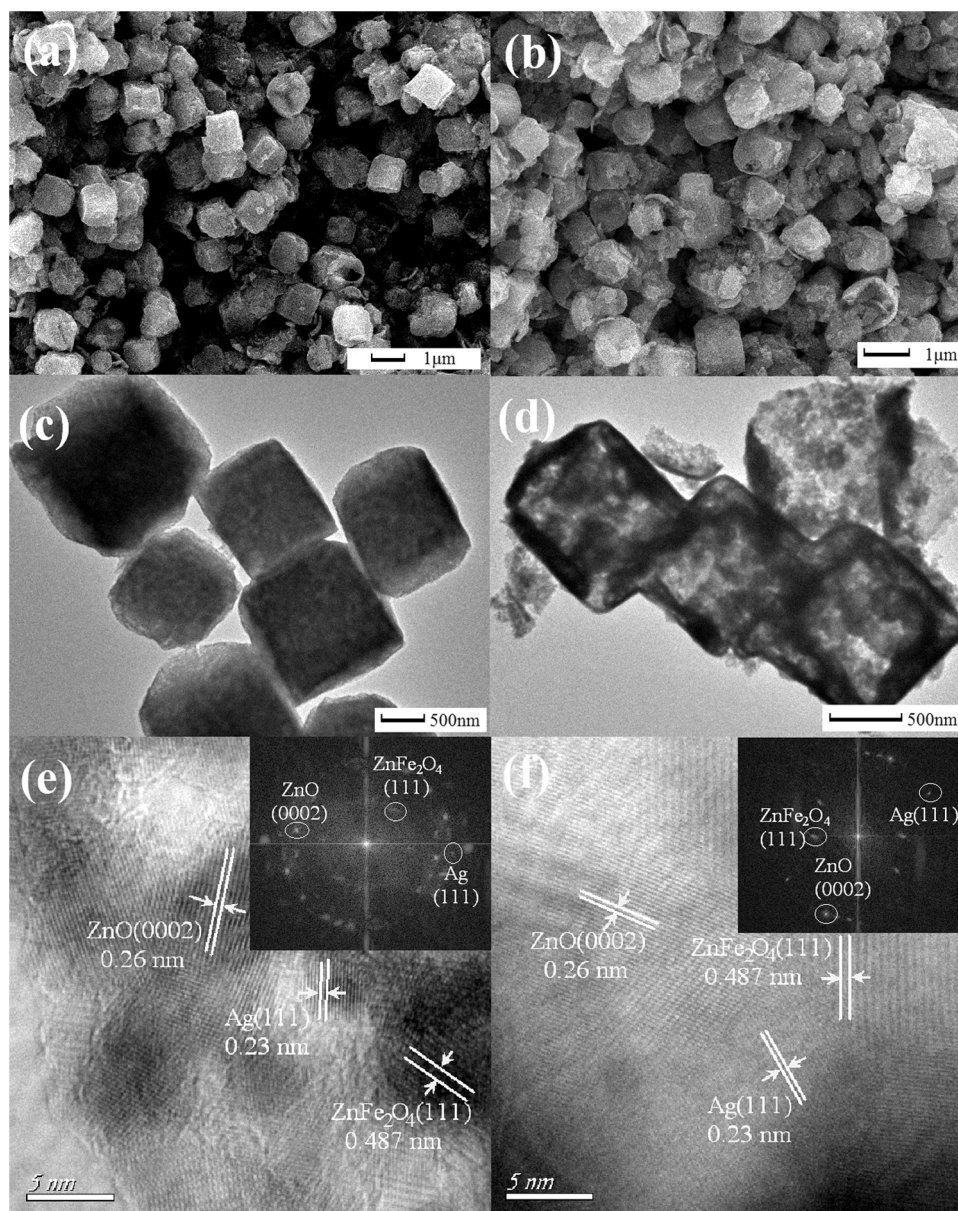


Fig. 2. FESEM, TEM and HRTEM images of (a, c, e) *p*-Ag/ZnO/ZnFe<sub>2</sub>O<sub>4</sub> and (b, d, f) *h*-Ag/ZnO/ZnFe<sub>2</sub>O<sub>4</sub>. The insets in (e) and (f) show the corresponding FFT patterns.

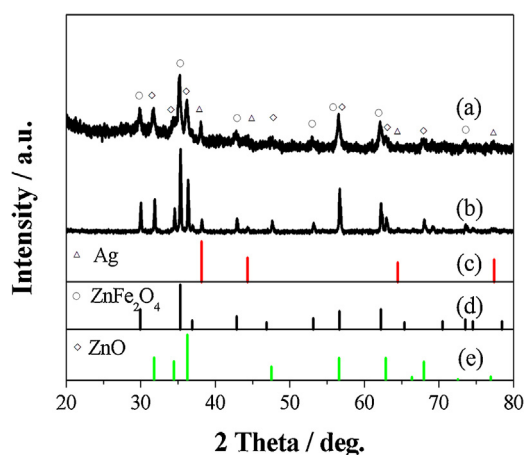


Fig. 3. XRD patterns of (a) *p*-Ag/ZnO/ZnFe<sub>2</sub>O<sub>4</sub> and (b) *h*-Ag/ZnO/ZnFe<sub>2</sub>O<sub>4</sub>. The standard patterns of (c) Ag, (d) ZnO and (e) ZnFe<sub>2</sub>O<sub>4</sub> are supplied for comparison.

*p*-Ag/ZnO/ZnFe<sub>2</sub>O<sub>4</sub> and *h*-Ag/ZnO/ZnFe<sub>2</sub>O<sub>4</sub>. Obviously, the diffractions peaks can be indexed to three components: the peaks marked with “Δ” correspond to the fcc Ag (JCPDS No. 65-2871), the peaks marked with ‘◇’ are in agreement with the hexagonal structure of ZnO (JCPDS No. 36-1451), while the peaks marked with ‘○’ can be ascribed to cubic structured ZnFe<sub>2</sub>O<sub>4</sub> (JCPDS No. 22-1012). The results unambiguously demonstrate that the obtained products consist of ZnFe<sub>2</sub>O<sub>4</sub>, ZnO and Ag, confirming the composition of *p*-Ag/ZnO/ZnFe<sub>2</sub>O<sub>4</sub> and *h*-Ag/ZnO/ZnFe<sub>2</sub>O<sub>4</sub>.

EDS spectra (Fig. S1) of *p*-Ag/ZnO/ZnFe<sub>2</sub>O<sub>4</sub> and *h*-Ag/ZnO/ZnFe<sub>2</sub>O<sub>4</sub> clearly exhibit the presence of Zn, Fe, Ag and O elements, giving further evidence that the obtained products are a composite of Ag, ZnO and ZnFe<sub>2</sub>O<sub>4</sub>. The Ag content in the two Ag/ZnO/ZnFe<sub>2</sub>O<sub>4</sub> samples is similar, 2.17 wt% for *p*-Ag/ZnO/ZnFe<sub>2</sub>O<sub>4</sub> and 2.17 wt% for *h*-Ag/ZnO/ZnFe<sub>2</sub>O<sub>4</sub>. The distribution of Zn, Fe, Ag and O elements in the cubes is also determined by EDX elemental mapping. As shown in Fig. 4, the highly uniform distribution of Zn, Fe, Ag and O elements suggests that the components of ZnFe<sub>2</sub>O<sub>4</sub>, ZnO and Ag homogeneously distributed in the

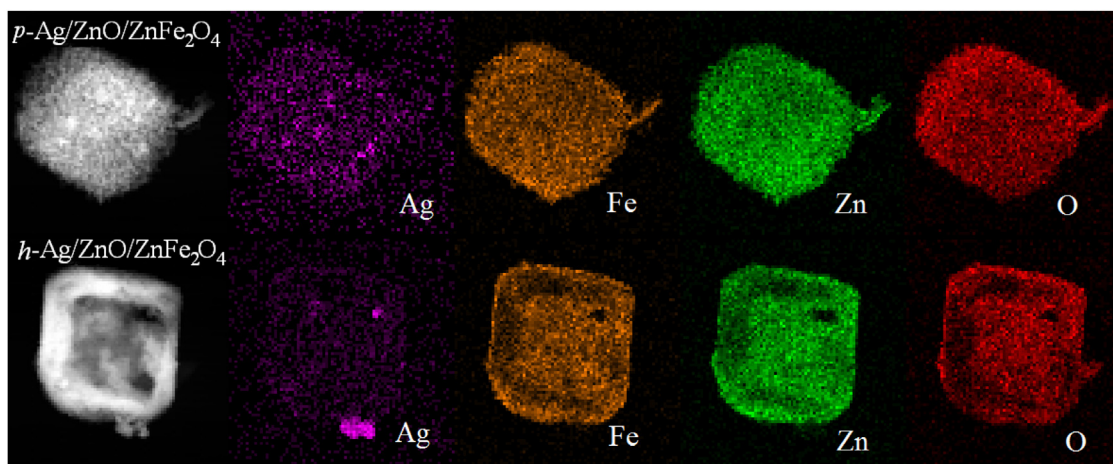


Fig. 4. The elemental mapping images of  $p\text{-Ag/ZnO/ZnFe}_2\text{O}_4$  and  $h\text{-Ag/ZnO/ZnFe}_2\text{O}_4$ .

composites. Therefore, the  $\text{Ag/ZnO/ZnFe}_2\text{O}_4$  ternary composites with highly uniform composition were obtained through the modified MOFs precursor approach.

The porosity of  $p\text{-Ag/ZnO/ZnFe}_2\text{O}_4$  and  $h\text{-Ag/ZnO/ZnFe}_2\text{O}_4$  products was further investigated by  $\text{N}_2$  adsorption–desorption measurements. Fig. 5 shows the  $\text{N}_2$  adsorption–desorption isotherm and the pore size distribution curve of the  $\text{Ag/ZnO/ZnFe}_2\text{O}_4$  samples. The BET surface areas of  $p\text{-Ag/ZnO/ZnFe}_2\text{O}_4$  and  $h\text{-Ag/ZnO/ZnFe}_2\text{O}_4$  are  $38.29$  and  $63.51 \text{ m}^2 \text{ g}^{-1}$ , respectively. The pore-size distribution obtained using the Barrett–Joyner–Halenda (BJH) method reveals a wide peak centered at ca.  $30 \text{ nm}$  for  $p\text{-Ag/ZnO/ZnFe}_2\text{O}_4$  (Fig. 5a), while a bimodal distribution with a narrow peak centered at  $8.3 \text{ nm}$  and a weak wide peak centered at  $25 \text{ nm}$  (Fig. 5b) is found for  $h\text{-Ag/ZnO/ZnFe}_2\text{O}_4$ . During the conversion process of the precursor to the composites, C and N were oxidized into gases and escaped, resulting in small pores sized at ca.  $8 \text{ nm}$ . Some of the small pores may connect with each other, leading to larger pores with a wide size distribution [30,31]. The results demonstrate that  $h\text{-Ag/ZnO/ZnFe}_2\text{O}_4$  possesses larger specific surface area and smaller pore size than  $p\text{-Ag/ZnO/ZnFe}_2\text{O}_4$ , which could exert an effect on their adsorption and catalysis performance.

As demonstrated above, with a facile calcination process, the  $\text{Ag-ZnPBA}$  precursor can be transformed into highly uniform  $\text{Ag/ZnO/ZnFe}_2\text{O}_4$  ternary composites, and the microstructure of the ternary composites can be tuned from porous to hollow by simply controlling the heating modes. As shown in Scheme 1, porous cubes were obtained by a rapid one-step heating process, while hollow ones were achieved by a slow two-step heating process. When with the fast heating rate, the quick release of  $\text{CO}_2$ ,  $\text{N}_2$ , and  $\text{H}_2\text{O}$  makes the cubes shrink inward, which induces the formation of porous structure. In contrast, at lower temperature with slow heating rate, the particles are first dehydrated and some channels formed due to the outward diffusion of water molecules. During the followed decomposition process at relatively higher temperature, the diffusion of air becomes easier, and oxygen is easier to enter into the particles' interior, which promotes the decomposition of cyanide. At the same time, the generated  $\text{CO}_2$  and  $\text{N}_2$  gases diffuse outwards. As a result, hollow structured particles are formed. With the same subsection heating process,  $\text{ZnO/ZnFe}_2\text{O}_4$  binary composite hollow cubes are also obtained using  $\text{ZnPBA}$  cubes as the precursor. The XRD pattern, FESEM, TEM and HRTEM images of the as-synthesized  $\text{ZnO/ZnFe}_2\text{O}_4$  hollow cubes are shown in Fig. S2.

Considering that  $\text{ZnO}$  as an amphoteric oxide can be dissolved by  $\text{NaOH}$  solution,  $\text{Ag/ZnFe}_2\text{O}_4$  composite was prepared by treating  $h\text{-Ag/ZnO/ZnFe}_2\text{O}_4$  with  $\text{NaOH}$  aqueous solution. The structural

and morphological characterizations of  $\text{Ag/ZnFe}_2\text{O}_4$  are shown in Fig. S3. The XRD pattern (Fig. S3a) reveals that the as-synthesized sample can be identified as a composite of  $\text{Ag}$  (JCPDS No. 65–2811) and  $\text{ZnFe}_2\text{O}_4$  (JCPDS No. 22–1012), confirming that the  $\text{Ag/ZnFe}_2\text{O}_4$  composite was obtained. The SEM image (Fig. S3b) shows that the cubic morphology of the  $\text{Ag/ZnFe}_2\text{O}_4$  is maintained after removing  $\text{ZnO}$ . The BET adsorption–desorption analysis and the BJH pore size distribution of  $\text{Ag/ZnFe}_2\text{O}_4$  (Fig. S4) reveal the larger BET surface area of  $95.23 \text{ m}^2 \text{ g}^{-1}$  and a broader pore-size distribution as compared with the original  $h\text{-Ag/ZnO/ZnFe}_2\text{O}_4$ .

### 3.2. Photocatalytic property

The optical absorption properties of the synthesized samples were probed by UV–vis diffuse reflectance spectroscopy. As shown in Fig. S5, the  $\text{ZnO/ZnFe}_2\text{O}_4$  sample exhibits significant visible-light absorption with absorption onset at ca.  $700 \text{ nm}$ , which corresponds well with that of the reported  $\text{ZnFe}_2\text{O}_4$ -doping  $\text{ZnO}$  [12]. After doped with  $\text{Ag}$  nanoparticles, the obtained  $\text{Ag/ZnO/ZnFe}_2\text{O}_4$  composites show enhanced visible-light absorption performance, which can be ascribed to the characteristic surface plasmon resonance absorption of the  $\text{Ag}$  nanoparticles [32]. The  $h\text{-Ag/ZnO/ZnFe}_2\text{O}_4$  with hollow structure shows the strongest light absorption, which is well consistent with its excellent photocatalytic activity as shown hereinafter.

To demonstrate the photocatalytic activity of the obtained  $\text{ZnFe}_2\text{O}_4$ -based materials, photocatalytic degradation of MB solution was carried out as a probe reaction under simulated sunlight irradiation. As shown in Fig. 6a, the photocatalytic activity increases in the order of  $\text{ZnO/ZnFe}_2\text{O}_4$ ,  $\text{Ag/ZnFe}_2\text{O}_4$ ,  $p\text{-Ag/ZnO/ZnFe}_2\text{O}_4$  and  $h\text{-Ag/ZnO/ZnFe}_2\text{O}_4$ . The  $\text{ZnO/ZnFe}_2\text{O}_4$  catalyst shows the poorest photodegradation efficiency, and only 20% of MB solution was degraded with 100 min irradiation. The  $\text{Ag/ZnFe}_2\text{O}_4$  shows better photocatalytic activity, and the corresponding degradation efficiency reaches 43%. In contrast, the ternary composites show significantly improved degradation efficiency compared to the binary composites, and the values reach 60% and 93% for  $p\text{-Ag/ZnO/ZnFe}_2\text{O}_4$  and  $h\text{-Ag/ZnO/ZnFe}_2\text{O}_4$ , respectively. Assuming that the degradation process obeys the first-order kinetics ( $c = c_0 e^{-kt}$ ,  $k$  is the photodegradation rate constant), the plots of  $\ln(c/c_0)$  as a function of the irradiation time  $t$  are shown in Fig. 6b. The derived parameters including  $k$  ( $\text{min}^{-1}$ ) and correlation coefficient  $R^2$  are listed in Table S1. Indeed, the photodegradation behaviors of MB solution on these catalysts obey the first-order kinetics. The  $h\text{-Ag/ZnO/ZnFe}_2\text{O}_4$  product shows the best photocatalytic activity among all these catalysts. The  $k$  value for



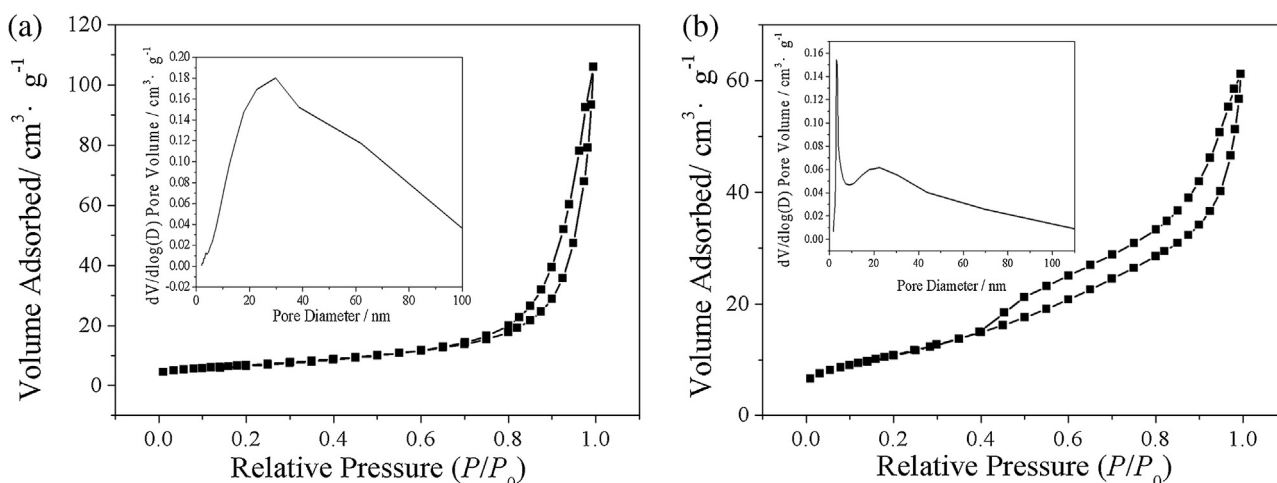
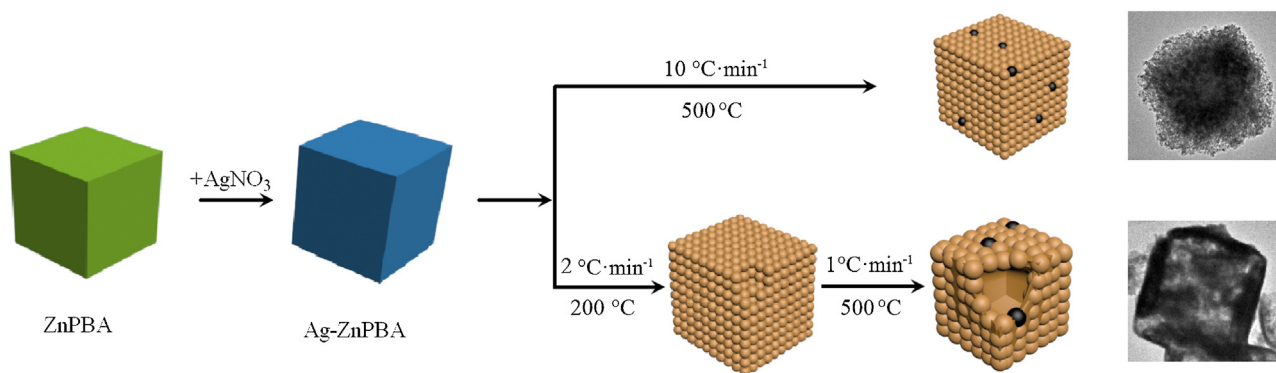


Fig. 5. BET adsorption–desorption analysis of (a) *p*-Ag/ZnO/ZnFe<sub>2</sub>O<sub>4</sub> and (b) *h*-Ag/ZnO/ZnFe<sub>2</sub>O<sub>4</sub>. The insets show the corresponding BJH pore size distributions.



Scheme 1. Schematic illustration of the formation of hollow/porous cubes of Ag/ZnO/ZnFe<sub>2</sub>O<sub>4</sub>.

*h*-Ag/ZnO/ZnFe<sub>2</sub>O<sub>4</sub> (0.021 min<sup>-1</sup>) is 2.8 times of *p*-Ag/ZnO/ZnFe<sub>2</sub>O<sub>4</sub> (0.0076 min<sup>-1</sup>), 6.4 times of Ag/ZnFe<sub>2</sub>O<sub>4</sub> (0.0033 min<sup>-1</sup>) and 12.4 times of ZnO/ZnFe<sub>2</sub>O<sub>4</sub> (0.0017 min<sup>-1</sup>). This suggests that the ternary Ag/ZnO/ZnFe<sub>2</sub>O<sub>4</sub> composite and the hollow nanostructure are beneficial for improving the photocatalytic performance due to the synergistic effect among the different components and the larger specific surface area (63.51 m<sup>2</sup> g<sup>-1</sup>), which can reduce the recombination of charge carriers and provide sufficient photocatalytic active sites.

In order to investigate the effect of silver loading amounts on the catalytic activity of Ag/ZnO/ZnFe<sub>2</sub>O<sub>4</sub> composites, the AgNO<sub>3</sub> solution used in the experiment was changed to 0.75, 3.0 and 4.0 mL. These contrast samples were synthesized under the same conditions as that of *h*-Ag/ZnO/ZnFe<sub>2</sub>O<sub>4</sub> and designated as *h*-Ag/ZnO/ZnFe<sub>2</sub>O<sub>4</sub>-1, *h*-Ag/ZnO/ZnFe<sub>2</sub>O<sub>4</sub>-2 and *h*-Ag/ZnO/ZnFe<sub>2</sub>O<sub>4</sub>-3, respectively. EDS spectra (Fig. S6) reveal that the Ag contents in *h*-Ag/ZnO/ZnFe<sub>2</sub>O<sub>4</sub>-1, *h*-Ag/ZnO/ZnFe<sub>2</sub>O<sub>4</sub>-2 and *h*-Ag/ZnO/ZnFe<sub>2</sub>O<sub>4</sub>-3 are about 1.15 wt%, 2.70 wt% and 3.94 wt%, respectively. The photocatalytic properties of the Ag/ZnO/ZnFe<sub>2</sub>O<sub>4</sub> composites with different Ag contents were investigated by the degradation of MB solution. As shown in Fig. 6c and d, the photodegradation rate of MB first increases with increasing Ag content from 1.15 wt% (*h*-Ag/ZnO/ZnFe<sub>2</sub>O<sub>4</sub>-1) to 2.17 wt% (*h*-Ag/ZnO/ZnFe<sub>2</sub>O<sub>4</sub>), and then decreases with further increasing the Ag content to 2.70 wt% (*h*-Ag/ZnO/ZnFe<sub>2</sub>O<sub>4</sub>-2) and 3.94 wt% (*h*-Ag/ZnO/ZnFe<sub>2</sub>O<sub>4</sub>-3). The degradation processes obey the first-order kinetics (Fig. 6d), and the *k* values increase in the order of *h*-Ag/ZnO/ZnFe<sub>2</sub>O<sub>4</sub>-3, *h*-Ag/ZnO/ZnFe<sub>2</sub>O<sub>4</sub>-1, *h*-Ag/ZnO/ZnFe<sub>2</sub>O<sub>4</sub>-2,

and *h*-Ag/ZnO/ZnFe<sub>2</sub>O<sub>4</sub> (Table S1). This result demonstrates that Ag content has an important influence on the photocatalytic activity of Ag/ZnO/ZnFe<sub>2</sub>O<sub>4</sub> composites, and *h*-Ag/ZnO/ZnFe<sub>2</sub>O<sub>4</sub> product with Ag content of 2.17 wt% shows the best photocatalytic performance. The photocatalytic activity caused by different Ag contents agree with the reported Ag-loaded TiO<sub>2</sub>, in which the work function of Ag nanoparticles is proposed to have a major influence on their photocatalytic performance [33].

TOC analysis confirms the mineralization involved in this photocatalytic decomposition of MB [34]. As shown in Fig. S7, under the simulated sunlight irradiation for 160 min, *h*-Ag/ZnO/ZnFe<sub>2</sub>O<sub>4</sub> exhibits a TOC removal rate of 87%, suggesting that mineralization process occurred in the decomposition of MB, and MB can be completely photodegraded by the Ag/ZnO/ZnFe<sub>2</sub>O<sub>4</sub> catalysts.

To evaluate the stability and reusability of the catalysts, a recyclability test of photodegradation MB solution with *h*-Ag/ZnO/ZnFe<sub>2</sub>O<sub>4</sub> was further performed. As shown in Fig. 7a, after five photodegradation cycles, the catalyst only exhibits a small loss of the activity, indicating its good stability for repeated photocatalysis. Fig. 7b shows the magnetic hysteresis loop of *h*-Ag/ZnO/ZnFe<sub>2</sub>O<sub>4</sub>, demonstrating a superparamagnetic behavior. As shown in the illustration of Fig. 7b, when a magnet approaches the reaction solution, *h*-Ag/ZnO/ZnFe<sub>2</sub>O<sub>4</sub> particles can be attracted to the sidewall of the magnet within a short time, and the solution becomes clear and transparent. This demonstrates that the Ag/ZnO/ZnFe<sub>2</sub>O<sub>4</sub> catalysts can be easily separated and enriched by an external magnetic field.

The excellent photocatalytic activity of the synthesized Ag/ZnO/ZnFe<sub>2</sub>O<sub>4</sub> nanocomposites motivated us to investigate

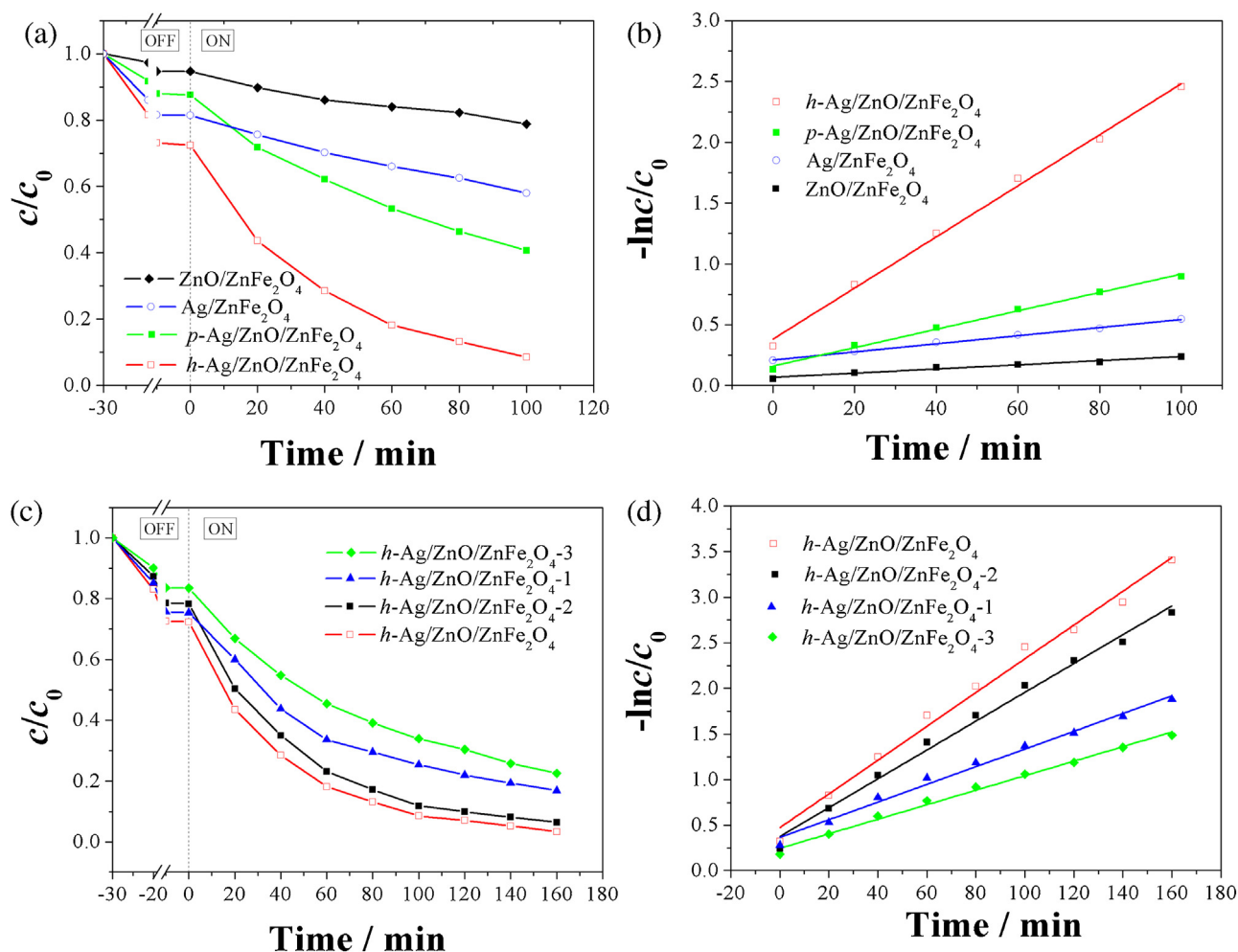


**Fig. 6.** (a) Photodegradation of MB solution and (b) pseudo-first-order plots of  $-\ln(c/c_0)$  vs.  $t$  under different catalysts. (c) Photodegradation of MB solution and (d) pseudo-first-order plots of  $-\ln(c/c_0)$  vs.  $t$  in the presence of ternary Ag/ZnO/ZnFe<sub>2</sub>O<sub>4</sub> hollow cubes with different Ag loading amounts.

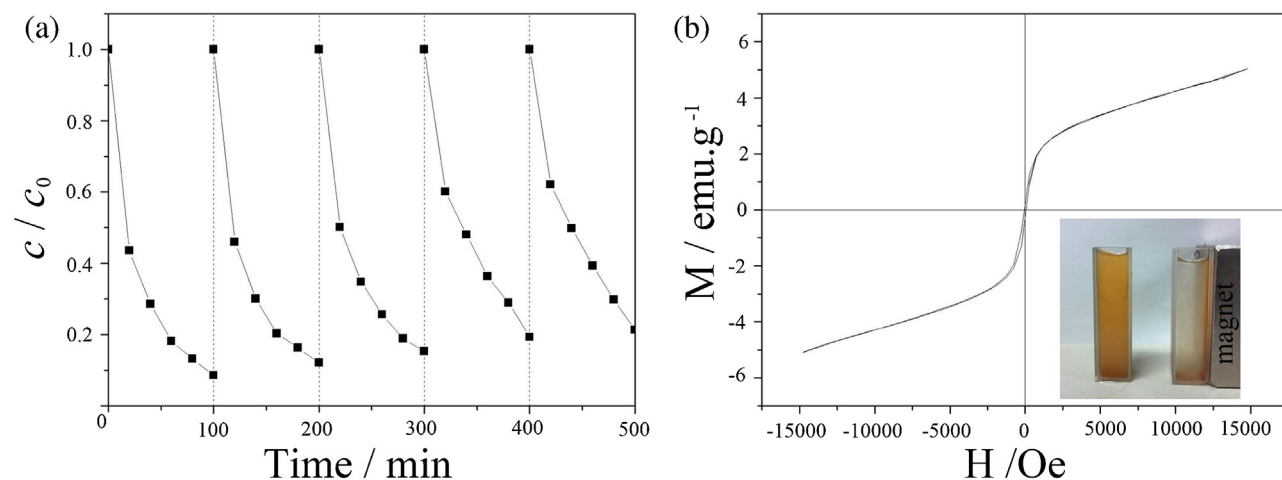


**Fig. 7.** (a) Cycling tests of *h*-Ag/ZnO/ZnFe<sub>2</sub>O<sub>4</sub> photocatalyst under simulated sunlight. (b) Magnetic hysteresis loop of *h*-Ag/ZnO/ZnFe<sub>2</sub>O<sub>4</sub> composite at 300 K. The inset shows the magnetic separation of the photocatalyst.

the photocatalytic mechanism of the degradation process. It is well known that active species such as holes, hydroxyl radicals ( $\cdot\text{OH}$ ), and superoxide radicals ( $\text{O}_2^{\cdot-}$ ) are usually involved in the photodegradation process [35]. To investigate the main active species and to further insight into the underlying photocatalytic mechanism, three different chemicals of EDTANa<sub>2</sub> (a hole

scavenger), *tert*-butyl alcohol (*t*-BuOH, a  $\cdot\text{OH}$  radical scavenger) and *p*-benzoquinone (BZQ, a  $\text{O}_2^{\cdot-}$  radical scavenger) were introduced into the reaction systems, respectively [36,37]. As shown in Fig. S8, the rate constants for HC-2 in the presence of *t*-BuOH, BZQ and EDTANa<sub>2</sub> were estimated to be 0.0209, 0.0127, and 0.0066 min<sup>-1</sup>, respectively. Therefore, the introduction of EDTANa<sub>2</sub>

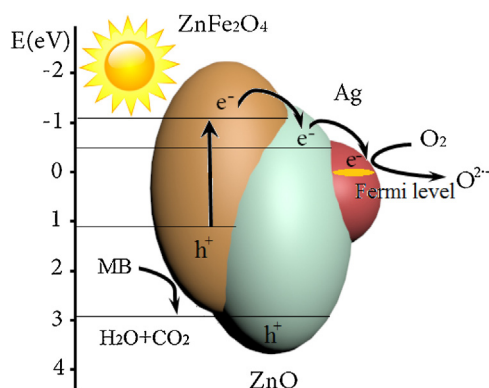


**Fig. 8.** The proposed degradation mechanism of organic pollutants over Ag/ZnO/ZnFe<sub>2</sub>O<sub>4</sub> photocatalysts.

and BZQ caused a remarkable decrease in the photocatalytic activity, whereas the presence of *t*-BuOH had no deleterious effect on the photocatalytic efficiency. These results suggest that direct hole and O<sub>2</sub><sup>•−</sup> radicals oxidation govern the photocatalytic process, and •OH radical was not the main active oxidative species in the photocatalytic degradation of MB solution.

The possible interfacial charge transfer process in the silver-modified semiconductors during dye degradation was presented in Fig. 8. As a narrow band gap semiconductor, ZnFe<sub>2</sub>O<sub>4</sub> can absorb visible light [1]. However, due to the rapid recombination of photo-generated electrons and holes, ZnFe<sub>2</sub>O<sub>4</sub> usually shows rather poor photocatalytic activities [38]. Both the conduction band (CB) and valence band (VB) of ZnFe<sub>2</sub>O<sub>4</sub> are less negative compared with those of ZnO. When ZnO and ZnFe<sub>2</sub>O<sub>4</sub> are coupled together forming ZnO/ZnFe<sub>2</sub>O<sub>4</sub> composite, a type-II band alignment is formed. Consequently, the photogenerated electron-hole pairs in ZnFe<sub>2</sub>O<sub>4</sub> can be separated efficiently. The electrons are driven to CB of ZnO and the holes are left in the VB of ZnFe<sub>2</sub>O<sub>4</sub>.

When ZnO was modified by metallic silver, part of photogenerated electrons transferred from CB of ZnO to the surface of silver and was trapped by silver due to the formation of Schottky barrier between ZnO and Ag [39]. The work function of ZnO is about 5.2 eV and its first electron affinity is about 4.3 eV, while the work func-

tion of Ag is about 4.26 eV [40,41]. Thus the Fermi energy level of ZnO is lower than that of Ag because of the larger work function of ZnO. This results in the transfer of electrons from Ag to ZnO until the two systems attain equilibrium and form the new Fermi energy level ( $E_f$ ) [42,43]. This electron transfer will continue until the overall Fermi level of the metal-modified ZnO system shifts toward more negative potential and ultimately equilibrates with that of Ag [44–46]. Because the energy level of the CB for semiconductor ZnO is higher than the newly formed Fermi energy level  $E_f$ , the photogenerated electrons are transferred to the metallic Ag. Then the electrons in Ag component can be trapped by the chemisorbed O<sub>2</sub> to form the superoxide radicals. As a result, the recombination rate of photogenerated electrons and holes decreased considerably. Therefore, the loading of Ag and ZnO on ZnFe<sub>2</sub>O<sub>4</sub> is highly beneficial to the photocatalytic performance. Several groups have demonstrated that with higher metal content than the optimized one, the over-accumulations of electrons on metal deposits could attract the photogenerated holes to the metal sites. This may encourage the recombination of charge carriers and the metal deposits reversely behave as recombinant centers [47–50]. This is well consistent with our experimental result reported here.

Photocurrent response has recently been applied to investigate the separation efficiency of photogenerated electron-hole pairs in semiconductors [51]. Fig. 9 shows the photocurrent of *p*-Ag/ZnO/ZnFe<sub>2</sub>O<sub>4</sub>, *h*-Ag/ZnO/ZnFe<sub>2</sub>O<sub>4</sub>, Ag/ZnFe<sub>2</sub>O<sub>4</sub>, and ZnO/ZnFe<sub>2</sub>O<sub>4</sub> samples under the irradiation of a 500 W Xe lamp. It can be observed that ZnO/ZnFe<sub>2</sub>O<sub>4</sub> and Ag/ZnFe<sub>2</sub>O<sub>4</sub> exhibit weak photocurrent response signals. The photocurrent response of ternary Ag/ZnO/ZnFe<sub>2</sub>O<sub>4</sub> composites is stronger than that of binary composites. The results indicate that the surface recombination of the photogenerated electron-hole pairs in Ag/ZnO/ZnFe<sub>2</sub>O<sub>4</sub> is significantly suppressed; or the photogenerated electron-hole pairs are efficiently separated and transferred by the combination of the Ag, ZnO, and ZnFe<sub>2</sub>O<sub>4</sub>. Interestingly, the hollow nanostructure shows more excellent photocurrent response than the porous one. As shown in Fig. 9, the *h*-Ag/ZnO/ZnFe<sub>2</sub>O<sub>4</sub> nanocomposite shows the highest photocurrent response intensity, demonstrating that the surface recombination rate of the sample *h*-Ag/ZnO/ZnFe<sub>2</sub>O<sub>4</sub> is the lowest, which is in good agreement with the trend in the photocatalytic activity of the Ag/ZnO/ZnFe<sub>2</sub>O<sub>4</sub> nanocomposites.

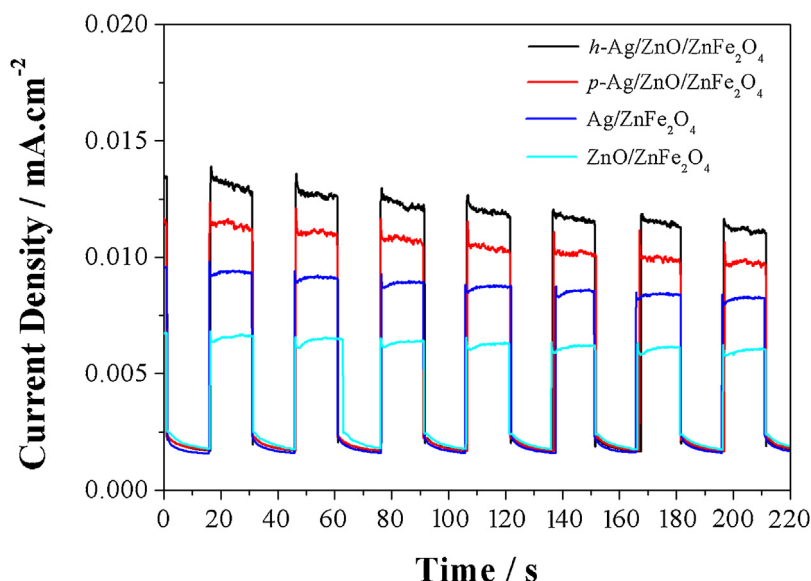


**Fig. 9.** Photocurrent response of *h*-Ag/ZnO/ZnFe<sub>2</sub>O<sub>4</sub>, *p*-Ag/ZnO/ZnFe<sub>2</sub>O<sub>4</sub>, Ag/ZnFe<sub>2</sub>O<sub>4</sub> and ZnO/ZnFe<sub>2</sub>O<sub>4</sub>.



#### 4. Conclusion

In conclusion, Ag/ZnO/ZnFe<sub>2</sub>O<sub>4</sub> porous and hollow nanocubes were synthesized using Ag-ZnPBA precursor through the controlled calcination processes. The photodegradation activities of Ag/ZnO/ZnFe<sub>2</sub>O<sub>4</sub> hollow cubes were demonstrated to be superior to those of the porous Ag/ZnO/ZnFe<sub>2</sub>O<sub>4</sub>, ZnO/ZnFe<sub>2</sub>O<sub>4</sub> or Ag/ZnFe<sub>2</sub>O<sub>4</sub> cubes. The new hybrid nanocomposites could effectively separate and transport photo-generated carriers by the type-II band alignment and Schottky barrier. Furthermore, Ag/ZnO/ZnFe<sub>2</sub>O<sub>4</sub> nanocomposites could be conveniently separated and recycled by using a magnet, which is very beneficial for practical applications. This study implies that the synthesis of multicomponent functional nanostructured materials could become more programmable using the modified MOFs as precursors, not only with controllable morphology and size, but also with adjustable composition, which would provide huge opportunities for environment and energy applications.

#### Acknowledgments

The authors are grateful for financial support from the National Natural Science Foundation of China (no. 51272094, 51072071, 81503351), the Doctoral Innovation Program Foundation of Jiangsu Province (KYLX\_1026), the Natural Science Foundation of Inner Mongolia (2012MS1209), Natural Science Foundation of Jiangsu province (No. BK20150507).

#### Appendix A. Supplementary data

Supplementary data associated with this article can be found, in the online version, at <http://dx.doi.org/10.1016/j.apcatb.2015.11.035>.

#### References

- [1] X. Cao, L. Gu, X. Lan, C. Zhao, D. Yao, W. Sheng, *Mater. Chem. Phys.* 106 (2007) 175.
- [2] R. Shao, L. Sun, L. Tang, Z. Chen, *Chem. Eng. J.* 217 (2013) 185.
- [3] Y. Fu, X. Wang, *Ind. Eng. Chem. Res.* 50 (2011) 7210.
- [4] Y. Sun, W. Wang, L. Zhang, S. Sun, E. Gao, *Mater. Lett.* 98 (2013) 124.
- [5] X. Li, Y. Hou, Q. Zhao, W. Teng, X. Hu, G. Chen, *Chemosphere* 82 (2011) 581.
- [6] H. Lv, L. Ma, P. Zeng, D. Ke, T. Peng, *J. Mater. Chem.* 20 (2010) 3665.
- [7] X. Chen, S. Shen, L. Guo, S. Mao, *Chem. Rev.* 110 (2010) 6503.
- [8] J. Di, J. Xia, Y. Ge, H. Li, H. Ji, H. Xu, Q. Zhang, H. Li, M. Li, *Appl. Catal. B Environ.* 168 (2015) 51.
- [9] C. Chen, Y. Liang, W. Zhang, *J. Alloys Compd.* 501 (2010) 168.
- [10] Y. Yao, J. Qin, Y. Cai, F. Wei, F. Lu, S. Wang, *Environ. Sci. Pollut. R.* 21 (2014) 7296.
- [11] Y. Hou, X. Li, Q. Zhao, X. Quan, G. Chen, *Adv. Funct. Mater.* 20 (2010) 2165.
- [12] L. Sun, R. Shao, L. Tang, Z. Chen, *J. Alloys Compd.* 564 (2013) 55.
- [13] X. Guo, H. Zhu, Q. Li, *Appl. Catal. B Environ.* 160 (2014) 408.
- [14] I. Arabatzi, T. Stergiopoulos, M. Bernard, D. Labou, S. Neophytides, P. Falaras, *Appl. Catal. B Environ.* 42 (2003) 187.
- [15] R. Georgekutty, M.K. Seery, S.C. Pillai, *J. Phys. Chem. C* 112 (2008) 13563.
- [16] L. Zhang, H. Wu, X. Lou, *J. Am. Chem. Soc.* 135 (2013) 10664.
- [17] L. Hu, Q. Chen, *Nanoscale* 6 (2014) 1236.
- [18] Z. Wang, X. Li, H. Xu, Y. Yang, Y. Cui, H. Pan, Z. Wang, B. Chen, G. Qian, *J. Mater. Chem. A* 2 (2014) 12571.
- [19] C. Du, F. Bu, D. Jiang, Q. Zhang, *J. Jiang, CrystEngComm* 15 (2013) 10597.
- [20] T. Kim, K. Lee, J. Cheon, J. Lee, S. Joo, H. Moon, *J. Am. Chem. Soc.* 135 (2013) 8940.
- [21] Y. Yan, F. Du, X. Shen, Z. Ji, X. Sheng, H. Zhou, G. Zhu, *J. Mater. Chem. A* 2 (2014) 15875.
- [22] B. Kong, J. Tang, Z. Wu, J. Wei, H. Wu, Y. Wang, G. Zheng, D. Zhao, *Angew. Chem. Int. Ed.* 53 (2014) 2888.
- [23] L. Hu, P. Zhang, H. Zhong, X. Zheng, N. Yan, Q. Chen, *Chem. Eur. J.* 18 (2012) 15049.
- [24] J. Sun, Q. Xu, *Energy Environ. Sci.* 7 (2014) 2071.
- [25] L. Zhang, H.B. Wu, S. Madhavi, H.H. Hng, X.W. Lou, *J. Am. Chem. Soc.* 134 (2012) 17388.
- [26] L. Hu, N. Yan, Q.W. Chen, P. Zhang, H. Zhong, X.R. Zheng, Y. Li, X.Y. Hu, *Chem. Eur. J.* 18 (2012) 8971.
- [27] L. Hu, P. Zhang, Y.K. Sun, S.X. Bao, Q.W. Chen, *ChemPhysChem* 14 (2013) 3953.
- [28] Y. Chen, S. Cheng, H. Xia, Y. Min, *Colloid Surf. A Physicochem. Eng. Asp.* 436 (2013) 1140.
- [29] F. Sousa, M. Sousa, I. Oliveira, A. Oliveira, R. Cavalcante, P. Fecine, V. Neto, D. Keukeleire, N. Nascimento, *J. Environ. Manag.* 90 (2009) 3340.
- [30] M. Regi, F. Ballas, D. Arcos, *Angew. Chem. Int. Ed.* 46 (2007) 7548.
- [31] Y. Yan, F. Du, X. Shen, Z. Ji, H. Zhou, G. Zhu, *Dalton Trans.* 43 (2014) 17544.
- [32] W. Hu, X. Chen, G. Wu, Y. Lin, N. Qin, D. Bao, *Appl. Phys. Lett.* 101 (2012) 063501.
- [33] M. Sadeghi, W. Liu, T. Zhang, P. Stavropoulos, B. Levy, *J. Phys. Chem.* 100 (1996) 19466.
- [34] Y. Liu, W. Yao, D. Liu, R. Zong, M. Zhang, X. Ma, Y. Zhu, *Appl. Catal. B Environ.* 163 (2015) 547.
- [35] W. Li, D. Li, Y. Lin, P. Wang, W. Chen, X. Fu, Y. Shao, *J. Phys. Chem. C* 116 (2012) 3552.
- [36] X. Yang, H. Cui, Y. Li, J. Qin, R. Zhang, H. Tang, *ACS Catal.* 3 (2013) 363.
- [37] G. Liao, S. Chen, X. Quan, H. Yu, H. Zhao, *J. Mater. Chem.* 22 (2012) 2721.
- [38] S. Xu, D. Feng, W. Shangguan, *J. Phys. Chem. C* 113 (2009) 2463.
- [39] Y. Zhang, J. Mu, *Colloid Interface Sci.* 309 (2007) 478.
- [40] Y. Lai, M. Meng, Y. Yu, *Appl. Catal. B Environ.* 100 (2010) 491–501.
- [41] W. Lu, G. Liu, S. Gao, S. Xing, J. Wang, *Nanotechnology* 19 (2008) 445711.
- [42] A. Wood, M. Giersig, P. Mulvaney, *J. Phys. Chem. B* 105 (2001) 8810.
- [43] C. Cheng, A. Amini, C. Zhu, Z. Xu, H. Song, N. Wang, *Sci. Rep.* 4 (2014) 4181.
- [44] M. Jakob, H. Levanon, P. Kamat, *Nano Lett.* 3 (2003) 353.
- [45] H. Yoo, C. Bae, Y. Yang, S. Lee, M. Kim, H. Kim, Y. Kim, H. Shin, *Nano Lett.* 14 (2014) 4413.
- [46] T. Hirakawa, P. Kamat, *J. Am. Chem. Soc.* 127 (2005) 3928.
- [47] A. Sclafani, J.M. Herrmann, *J. Photochem. Photobiol. A* 113 (1998) 181.
- [48] X.F. You, F. Chen, J.L. Zhang, M. Anpo, *Catal. Lett.* 102 (2005) 247.
- [49] H. Tahiri, Y.A. Ichou, J.M. Herrmann, *J. Photochem. Photobiol. A* 114 (1998) 219.
- [50] I.M. Arabatzi, T. Stergiopoulos, D. Andreeva, S. Kitova, S.G. Neophytides, P. Falaras, *J. Catal.* 220 (2003) 127.
- [51] H. Lv, X. Shen, Z. Ji, K. Chen, G. Zhu, *New J. Chem.* 38 (2014) 2305.